Critical Scaling of Solid Fragmentation at Quasistatic and Finite Strain Rates

Joel T. Clemmer and Mark O. Robbins

Phys. Rev. Lett. **129**, 078002 — Published 11 August 2022

DOI: 10.1103/PhysRevLett.129.078002

Critical Scaling of Solid Fragmentation at Quasistatic and Finite Strain Rates

Joel T. Clemmer[1] and Mark O. Robbins[2]
[1]*Sandia National Laboratories, Albuquerque, New Mexico 87185, USA*
[2]*Department of Physics and Astronomy, Johns Hopkins University, Baltimore, Maryland 21218, USA*

Using two-dimensional simulations of sheared, brittle solids, we characterize the resulting fragmentation and explore its underlying critical nature. Under quasistatic loading, a power-law distribution of fragment masses emerges after fracture which grows with increasing strain. With increasing strain rate, the maximum size of a grain decreases and a shallower distribution is produced. We propose a scaling theory for distributions based on a fractal scaling of the largest mass with system size in the quasistatic limit or with a correlation length that diverges as a power of rate in the finite-rate limit. Critical exponents are measured using finite-size scaling techniques.

Under large forces, solids fracture and fragment. This process in which material breaks down into smaller components or comminution is relevant to many problems including the motion of tectonic plates [1, 2], asteroid collisions [3], ice floes [4, 5], ballistic armor [6–9], and high-pressure granular flow and compaction [10–12]. The extent of fragmentation is often measured through the distribution of the number of fragments N of mass M or $N(M)$ which is a common basis for continuum formulations of breakage mechanics [13–16]. Theoretical models developed to predict the evolution and final state of $N(M)$ [3, 17–19] have widespread application, including even seemingly disparate processes such as crumpling paper [20]. This creates a need for data and a comprehensive understanding of the dynamics of fragmentation to test and calibrate models.

Intriguingly, it is often observed in fragmented granular matter that $N(M)$ decays as a power of increasing M with an exponent τ, $N(M) \sim M^{-\tau}$ [21]. This has been seen in experiments and simulations of impacted [22–25], crushed [26–29], and sheared [1, 30] solids. Fragmentation has therefore been postulated to be an instance of self-organized criticality [13, 22, 31], a theory that some systems can naturally evolve towards a critical state [32]. Scale-invariant behavior has been found in many other dynamic systems including sheared yield-stress materials [33–37] and depinning elastic interfaces [38–42] which respond to a slow driving rate with power-law distributed bursts of activity or avalanches and are each understood to represent a dynamical critical point [43–45]. In comparison, we have relatively little understanding of connections between fragmentation and criticality.

One puzzle is the value of τ which has been measured between 1.5 and 2.2 in different fragmented materials [21]. Different values of τ have also been identified in models of lattice stability [21, 46, 47] and simulations [23–25, 29, 31, 48, 49]. However, if fragmentation is an instance of critical behavior, one might expect all systems described by the same critical point to share a universal τ. It is unknown whether this could be explained by the existence of several distinct universality classes or by some alternate mechanism. Furthermore, it is unclear how a critical distribution develops with strain or how distributions depend on system size or strain rate which can truncate critical scaling.

In this article, we explore these questions using large, particle-based simulations of sheared, brittle solids in two-dimensions. By tracking the evolution of the mass distribution $N(M)$ with strain at different rates, we provide new insight into the dynamics of fragmentation. After fracture in the quasistatic limit, $N(M)$ has a power-law regime extending to an upper cutoff M_{cut} that grows with strain. At larger strain rates, the system enters a finite-rate regime where a rate-dependent M_{cut} emerges that shrinks with increasing rate. Unusual finite-rate effects are also identified in the evolution of $N(M)$ which may explain some variation in measured exponents. We present a scaling theory for $N(M)$ and test it using finite-size scaling analysis. The size of the largest grain grows as a power of system size in the quasistatic limit and as a power of decreasing rate in the finite-rate limit.

To create a minimal model of fragmentation, we use ideas from molecular dynamics and bonded particle models [50] based on early work by Maloney and Robbins [51]. Solids are represented as disordered packings of repulsive point particles connected by pairwise, attractive bonds that break under large tensile forces. Bonds have an equilibrium length equal to their initial length to create a stress-free reference state. All quantities in this letter are dedimensionalized using the diameter and mass of a particle and the energy scale of a bond. Appendix A includes details on the model and deformation protocol.

Under shear, solids fracture into separate fragments which continue to break down into smaller pieces during flow. This process results in polydisperse granular states illustrated in Fig. 1. Individual grains or fragments are identified as disconnected subgraphs in the network of unbroken bonds. To calculate the distribution $N(M)$, grains are logarithmically binned by mass M and each bin is normalized by its width, labeled by its upper cutoff, and averaged across multiple system realizations. Grains of mass $M < 3$ were not tallied. The ability to resolve the breakup of individual grains with strain during a simulation helps illuminate the process of fragmentation although advanced experimental techniques have also recently been used to track fracture in brittle materials [11, 52]. We first consider results from large systems with side lengths of $L = 2400$ containing

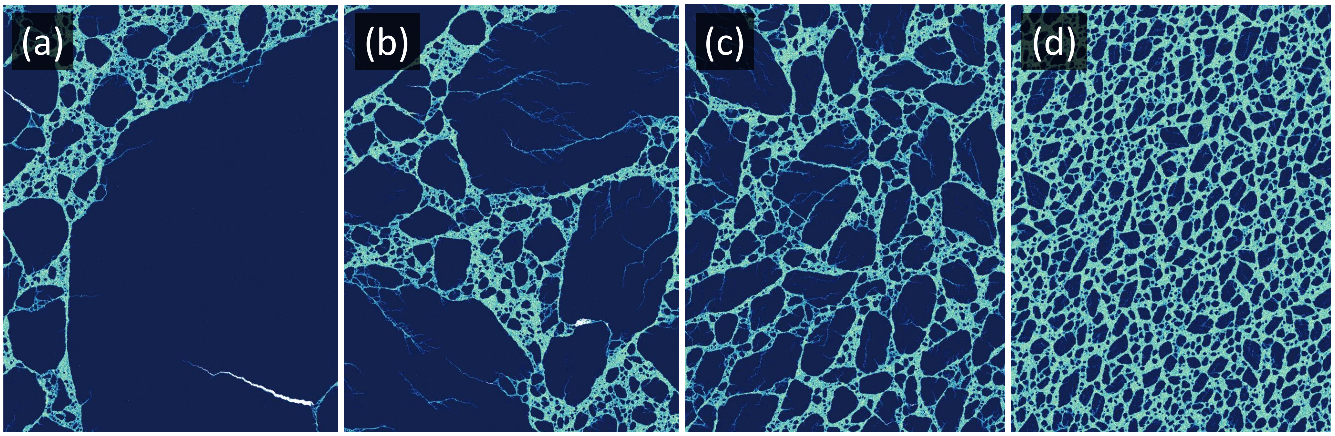

FIG. 1. Rendered sections of systems at 200% strain for rates of (a) $\dot{\epsilon} = 10^{-6}$, (b) 10^{-5}, (c) 10^{-4}, and (d) 10^{-3}. Particles are colored by the number of broken bonds interpolating from dark blue (no broken bonds) to pale yellow (all bonds broken).

$\sim 8 \times 10^6$ particles sheared at a strain rate of $\dot{\epsilon} = 10^{-6}$. This rate exemplifies the quasistatic (QS) limit as further reductions in rate do not affect results.

In Fig. 2(a), QS distributions $N(M)$ are plotted for various strains ϵ. Shortly after the system first fractures at $\epsilon = 2.2\%$, a power-law regime has already developed extending from a lower limit of $M_{\text{min}} \approx 10^2$ to an upper cutoff of $M_{\text{cut}} \approx 10^4$. Below M_{min}, there is an excess of small fragments as $N(M)$ rises even faster with decreasing M. The statistics of these small fragments are likely influenced by the limiting size of a particle and are not expected to display the same scaling. Above M_{cut}, $N(M)$ drops to zero before returning at an even larger mass of $M_{\text{max}} \approx 10^7$, implying most of the system is still intact. The early emergence of a power law reflects results from impacted brittle solids which broke into power-law distributed fragments despite limited material flow [22–25].

As ϵ increases, the number of fragments with $M < M_{\text{max}}$ increases. The power-law domain extends further as M_{cut} grows before saturating around 3×10^6 at $\epsilon = 100\%$ producing granular states similar to the system seen in Fig. 1(a). The flow of mass to smaller scales is fueled by a reduction in M_{max} which continues until $M_{\text{cut}} \approx M_{\text{max}}$. The continued breakage is consistent with experiments which found comminution persists to large strains in shear [1, 30]. At even larger ϵ (not shown), the repository of material at M_{max} is depleted and M_{cut} decays. $N(M)$ decreases for all $M > M_{\text{min}}$ as small grains constitute a larger fraction of mass. At $\epsilon = 100\%$ we estimate a power-law exponent $\tau = 1.70 \pm 0.08$, placing emphasis on larger M. In Fig. 2(b), data is multiplied by this power law to highlight minimal deviation at all ϵ. Over this range of ϵ, $N(M)$ also grows as a power of ϵ with an exponent of $\phi \approx 0.55 \pm 0.7$ such that curves collapse vertically in Fig. 2(b) after scaling by $\epsilon^{-\phi}$. The errorbars for exponents reflect the estimated range of values that reasonably describe the data.

A limited set of three-dimensional simulations were also run, described in the Supplemental Material, which exhibited qualitatively similar behavior with $\tau = 1.7 \pm 0.1$ [53]. These values of τ fall within the range of experimentally measured exponents in fragmented systems, $\tau \sim 1.5 - 2.2$ [21]. The origin of this variation is unknown, but several studies have identified potentially relevant variables. In ballistic impacts, τ depended on the initial geometry [22]. In simulations, τ may depend on plasticity [25], the extent of loading [29], and the rules of fracture [49]. Lattice models suggested fragility may affect τ [21]. We focus on the effect of strain rate.

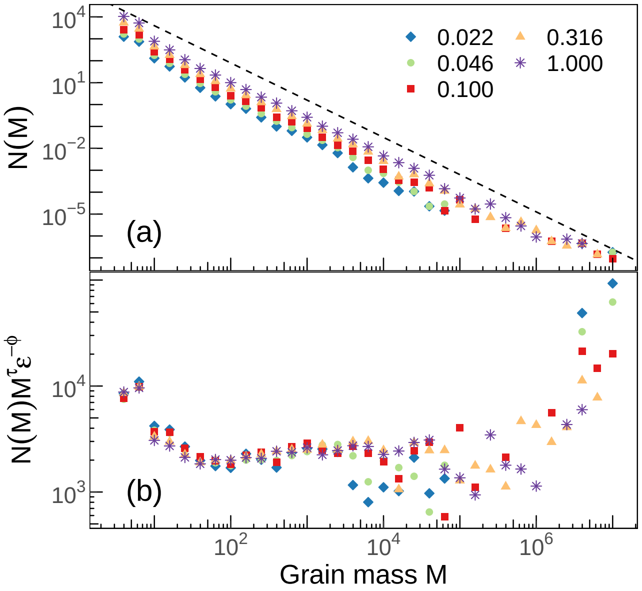

FIG. 2. (a) Quasistatic distributions $N(M)$ at the indicated strains ϵ. The dashed line represents a power law with exponent τ. (b) $N(M)$ scaled by the measured power law and ϵ^{ϕ}. Values of exponents are listed in Table I.

At high rates $\dot{\epsilon}$, the accelerated accumulation of stress must be relaxed by nucleating more cracks [55] producing a finer set of fragments [17, 23, 24, 56–58]. Correspondingly in our simulations, there is a rapid drop in the size

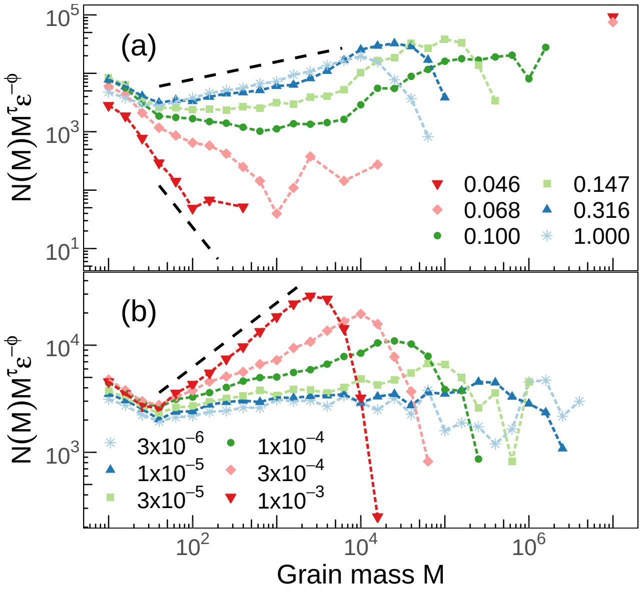

FIG. 3. (a) Scaled finite-rate distributions $N(M)$ sheared to the indicates strains ϵ at a rate of $\dot{\epsilon} = 3 \times 10^{-4}$. (b) Scaled $N(M)$ at $\epsilon = 100\%$ for the indicated $\dot{\epsilon}$. Dashed lines represent exponents δ equal to 1.8 and -0.3 in (a) and -0.6 in (b).

of the largest fragments with increasing $\dot{\epsilon}$ reflected in Fig. 1. This has a dramatic effect on the evolution of $N(M)$ with strain as seen for data at $\dot{\epsilon} = 3 \times 10^{-4}$ in Fig. 3(a). At small ϵ, $N(M)$ drops even faster with increasing N. While it would be difficult to claim this data is a power law, a different exponent $-(\tau + \delta)$ would be measured if a power law was fit with δ possibly as large as 1.8.

As ϵ increases, M_{max} decreases at a significantly faster pace and the growth in M_{cut} truncates at a lower value compared to QS data. Surprisingly, distributions become less steep such that a fitted δ would decrease with increasing ϵ and saturate around -0.3 at $\epsilon = 100\%$. While we cannot determine whether or not these curves are real power laws due to small and ambiguous domains, this highlights that fragmentation can have a dramatic dependence on rate and could possibly explain some variety in measured τ. Different exponents could be fit at high rates depending on the accumulated strain. Similar behaviors were seen in three-dimensional systems [53].

In Fig. 3(b), scaled distributions at $\epsilon = 100\%$ and different $\dot{\epsilon}$ demonstrate a clear growth in M_{cut} with decreasing $\dot{\epsilon}$ as distributions approach the QS limit. At these large strains, the potential power-law domain is less ambiguous and can rival those of many datasets conjectured to be power-law distributed [59]. This limit therefore has a stronger basis for a rate-dependent exponent with δ growing from -0.6 to zero with decreasing $\dot{\epsilon}$. Note that the rate of change in δ slows with decreasing $\dot{\epsilon}$ implying this effect becomes less significant at smaller $\dot{\epsilon}$.

To characterize the rate-dependence of M_{cut}, we consider finite-size effects at $\epsilon = 100\%$. At a QS rate $\dot{\epsilon} = 10^{-6}$, smaller systems with side lengths L have a smaller M_{cut} and have fewer grains as expected. In particular, we find in Fig. 4 that $N(M)$ scales as a power of L with an exponent γ and, focusing on large M, estimate $\gamma = 1.65 \pm 0.10$ which implies the number of grains does not grow extensively as L^2. There is also an additional spike near M_{cut} in small systems that disappears with increasing L.

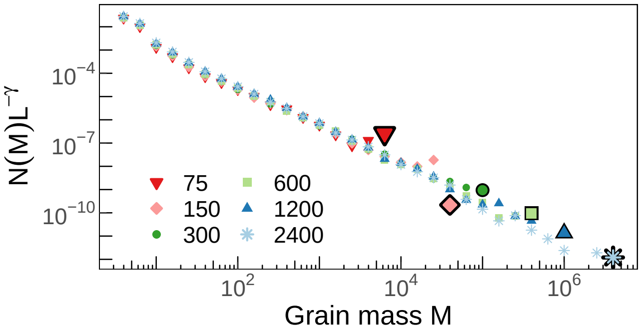

FIG. 4. Quasistatic distributions $N(M)$ scaled by L^{γ} with $\gamma = 1.65$ for the indicated system sizes L sheared at $\dot{\epsilon} = 10^{-6}$ to $\epsilon = 100\%$. The largest mass at each L is enlarged.

In contrast at a high rate of $\dot{\epsilon} = 10^{-3}$, $N(M)$ is independent of L. As $\dot{\epsilon}$ decreases, distributions for $L = 75$ first begin to deviate at $\dot{\epsilon} = 3 \times 10^{-4}$ as $N(M)$ stops evolving with further reductions in $\dot{\epsilon}$ and finite-size effects emerge. Larger systems with $L > 75$ similarly crossover to a QS limit at lower values of $\dot{\epsilon}$. Examples of this behavior are included in Appendix B. This observation reflects results from the aforementioned depinning and yielding transitions where QS driving allows a system to reach a critical state. At finite rates, these systems move away from the critical point and their dynamics are only correlated up to a correlation length ξ which decreases as a power of increasing rate [44, 45, 60–64].

In a similar vein, we postulate that there exists a diverging correlation length $\xi \sim \dot{\epsilon}^{-\nu}$ in fragmentation where ν is a new critical exponent. In infinitely large systems, ξ governs the maximum size of a fragment such that $M_{\mathrm{cut}} \sim \xi^{\alpha}$ where α is another exponent. In finite systems with $L > \xi$, L does not affect the maximum grain size and M_{cut} is equivalent to that of an infinite system. This is the finite-rate (FR) limit. In contrast if $L < \xi$, the maximum grain size is constrained by L and not ξ such that $M_{\mathrm{cut}} \sim L^{\alpha}$ and it is insensitive to further reductions in rate. This is the QS limit. To capture these ideas, we assume $N(M)$ only depends upon M/M_{cut} for $M > M_{\mathrm{min}}$ for sufficiently large ξ and L and construct two scaling ansatzes. In the QS limit,

$$N_{\mathrm{QS}}(M, L) \sim L^{\gamma - \alpha\tau} f(M/L^{\alpha}) \qquad (1)$$

where $f(x)$ is a scaling function that goes to zero for $x \gg 1$ and $f(x) \sim x^{-\tau}$ for $x \ll 1$ to recover $N_{\mathrm{QS}}(M) \sim L^{\gamma} M^{-\tau}$. In the FR regime, a d-dimensional system can be divided up into independent regions of size ξ^d each of which contain a distribution $N_{\xi}(M)$ of fragments. Assuming $N_{\xi}(M) \sim N_{\mathrm{QS}}(M, L = \xi)$, one can combine the

τ	1.70 ± 0.08	$N(M) \sim M^{-\tau}$
ϕ	0.55 ± 0.07	$N(M) \sim \epsilon^{\phi}$
γ	1.65 ± 0.1	$N(M) \sim L^{\gamma}$
α	1.7 ± 0.15	$M_{\mathrm{cut}} \sim L^{\alpha}, \xi^{\alpha}$
ν	0.70 ± 0.08	$\xi \sim \dot{\epsilon}^{-\nu}$

TABLE I. Estimates and definitions of critical exponents. Values are consistent with the scaling relation $\gamma+\alpha(2-\tau)=d$.

$(L/\xi)^d$ contributions to derive

$$N_{\mathrm{FR}}(M,\dot{\epsilon}) \sim L^d \dot{\epsilon}^{\nu(d-\gamma+\alpha\tau)} \mathcal{F}(M\dot{\epsilon}^{\nu\alpha}) \tag{2}$$

where $\mathcal{F}$ is a new function with the same limits as f.

In theory distributions in Figs. 4 and 3(b) can be collapsed using these expressions but this is complicated by deviations at small L and large $\dot{\epsilon}$ that violate assumptions as discussed in Appendix B. Alternatively, we consider integrated values of $N(M)$ which also highlight the crossover between the QS and FR regimes. Using Eq. (1), the n^{th} moment of $N_{\mathrm{QS}}(M,L)$ is

$$\langle M^n \rangle_{\mathrm{QS}} = \int M^n N_{\mathrm{QS}}(M,L) dM \sim L^{\gamma+\alpha(n+1-\tau)} \tag{3}$$

where integrals are dominated by the upper bound of M_{cut} for $n > \tau - 1 \approx 0.7$. Note that $N(M)$ is not normalized such that the first moment $\langle M \rangle$ is simply the total mass of fragments. Therefore, conservation of mass requires $\langle M \rangle \sim L^d$ implying $\gamma + \alpha(2-\tau) = d$. A similar scaling relation exists for avalanche distributions in the yielding transition [35, 36, 63]. Using this relation, Eq. (3) simplifies to $\langle M^n \rangle_{\mathrm{QS}} \sim L^{d+\alpha(n-1)}$. In the FR regime, $\langle M^n \rangle_{\mathrm{FR}} \sim L^d \dot{\epsilon}^{\nu\alpha(1-n)}$ is found by integrating Eq. (2).

As the first moment is trivial, we focus on the scaling of the second moment. In the inset of Fig. 5, $\langle M^2 \rangle L^{-d}$ does not depend on L at large $\dot{\epsilon}$ but grows as a power of decreasing $\dot{\epsilon}$ as predicted. However, this growth is immediately interrupted for the smallest system, $L = 75$, as finite-size effects emerge. As $\dot{\epsilon}$ continues to decrease, curves saturate at lower $\dot{\epsilon}$ for larger L reflecting the divergence in ξ. Assuming the only relevant length scales are ξ and L such that $\langle M^2 \rangle$ depends on the ratio L/ξ, we construct the finite-size scaling ansatz

$$\langle M^2 \rangle \sim L^{d+\alpha} g(\dot{\epsilon} L^{1/\nu}) \tag{4}$$

where $g(x)$ is a scaling function which must approach a constant at small x and $x^{-\nu\alpha}$ at large x to reproduce QS and FR scaling, respectively. Using this expression, data is collapsed in Fig. 5 with values of $\alpha = 1.7 \pm 0.15$ and $\nu = 0.70 \pm 0.08$. Although this collapse supports the proposed scaling theory, it also did not account for deviations identified at small L and high $\dot{\epsilon}$ which affect values of $\langle M^2 \rangle$. Future studies should focus on larger systems and slower rates which are expected to reduce deviations to validate estimates of exponents.

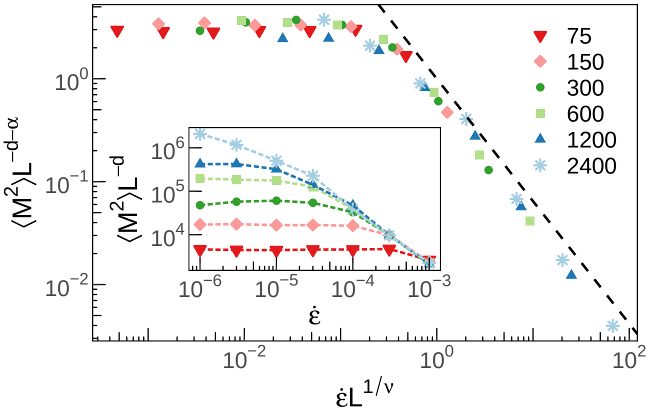

FIG. 5. The second moment $\langle M^2 \rangle$ as a function of rate $\dot{\epsilon}$ for the indicated system sizes L after scaling data using Eq. (4) and exponents in Table I. The dashed line represents a power law with exponent $-\nu\alpha$. The inset includes uncollapsed data.

This work provides a detailed study of fragmentation and new insight into the rate-dependent evolution of the grain size distribution $N(M)$ in shear. A power-law regime in $N(M)$ with exponent τ rapidly emerges after fracture in the quasistatic limit. With increasing strain, unfragmented material is consumed as mass flows to smaller length scales driving an extension of the power-law domain. For all M in this domain, $N(M)$ grows as a power of strain.

With increasing strain rate, fragments become finer as the power-law regime of $N(M)$ is truncated at a smaller, rate-dependent limit M_{cut} suggesting the system moves away from the critical quasistatic limit. The distribution also evolves differently as $N(M)$ decays more rapidly with N at small strains but becomes less steep with increasing strain. At large strains, masses still appear to be power-law distributed with a rate-dependent exponent The physical origin of this effect is unknown but it indicates that the relative strength of fragments of different sizes may depend on rate.

We propose the change in M_{cut} with rate is captured by a correlation length ξ that diverges as a power of decreasing rate. As ξ grows to exceed the system size L, finite-size effects emerge in $N(M)$ as the system enters the quasistatic limit. These ideas form the basis of a scaling theory for $N(M)$ which was verified using finite-size scaling analysis. A series of critical exponents, summarized in Table I, were measured which determine the size of the largest grain, the number of grains, and the divergence of the correlation length.

While this article has begun to characterize the rich size- and rate-dependence of fragmentation in shear, there are many more avenues to consider. Further work is needed to investigate the deviations to scaling seen at high rates and in small systems and test scaling theories in three-dimensions. It is also important to systematically explore other variables such as loading geometry, material properties, and inertia to identify their impact on fragmentation.

ACKNOWLEDGMENTS

Calculations were performed at the Maryland Advanced Research Computing Center, the DoD High Performance Computing Modernization Program, and at Sandia National Laboratories. Research was sponsored by the Army Research Laboratory and was accomplished under Cooperative Agreement Number W911NF-12-2-0022. The views and conclusions contained in this document are those of the authors and should not be interpreted as representing the official policies, either expressed or implied, of the Army Research Laboratory or the U.S. Government. The U.S. Government is authorized to reproduce and distribute reprints for Government purposes notwithstanding any copyright notation herein.

Sandia National Laboratories is a multi-mission laboratory managed and operated by National Technology and Engineering Solutions of Sandia, LLC., a wholly owned subsidiary of Honeywell International, Inc., for the U.S. Department of Energy's National Nuclear Security Administration under contract DE-NA-0003525. The views expressed in the article do not necessarily represent the views of the U.S. DOE or the United States Government.

Appendix A: Simulation details

To prepare systems, we generated disordered two-dimensional square packings of particles using a protocol from Refs. [63, 65] to ensure isotropic material properties. To prevent crystallization, particles are bidisperse with diameters of either a, the unit of length, or $3/5a$ and the ratio of the number of large to small particles is set to $(1+\sqrt{5})/4$. All particles have mass m. Two-dimensional simulations can be calibrated to represent plane-strain deformation and are relevant to thin sheets such as ice floes [4, 5] and exploded egg shells [66]. Unlike typical bonded particle models, particles do not have rotational degrees of freedom although rotation emerges in clusters of bonded particles. This reduces computational costs allowing larger systems to be simulated for longer times.

Bonds are created using a Delaunay triangulation generated from particle positions. Bonds are two-body central forces with magnitudes that depend on the distance between the two particles at the start of the simulation r_0 and at the current timestep r:

$$F_B = \begin{cases} 6 \times 2^{2/3} \frac{u r_0^2}{a^2 r} \left[\left(\frac{r_0}{r}\right)^{12} - \left(\frac{r_0}{r}\right)^{6} \right], & r \leq r_0 \\ C_1(r - r_0) + C_3(r - r_0)^3, & r_0 < r < \lambda r_0 \\ 0, & r \geq \lambda r_0 \end{cases} . \tag{A1}$$

In compression, this is a repulsive Lennard-Jones (LJ) force with an equilibrium distance of r_0 and a stiffness at small displacements of $36 \times 2^{2/3} u/a^2$, independent of r_0, where u is the unit of energy. In extension, the force is an attractive polynomial with coefficients C_1 and C_3 chosen to mirror the stiffness at $r = r_0$ and ensure a smooth transition to zero at $r = \lambda r_0$ where $\lambda = 1.05$ represents the limiting stretch where the bond permanently breaks.

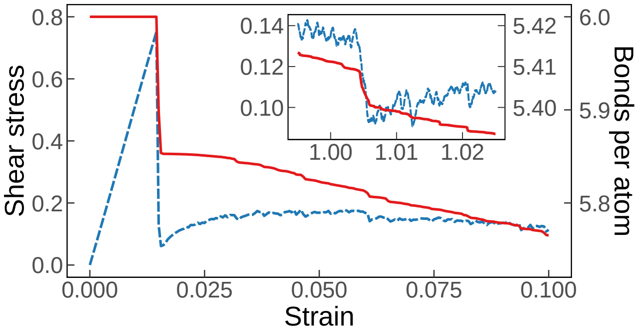

FIG. 6. Example curves of stress (blue, dashed) and the average number of bonds per atom (red, solid) versus strain. Data is from a system of linear size $L = 1600$ sheared at a rate $\dot{\epsilon} = 10^{-6}$. The inset includes a snapshot at higher strains.

Neighboring, non-bonded particles interact with a repulsive LJ force with an energy scale u. The force is truncated at its equilibrium distance which is set equal to the sum of particle radii. A Galilean-invariant damping force, similar to that used in dissipative particle dynamics [67], is applied to all pairs of interacting particles with a magnitude of

$$F_D = -\Gamma \left(1 - \frac{r}{r_{\max}}\right)^2 (\hat{r} \cdot \delta\vec{v}) \tag{A2}$$

where $\hat{r}$ is the unit vector between the two particles, $\delta\vec{v}$ is the difference in velocities, and $r_{\max}$ represents the maximum interaction distance, either λr_0 for bonded particles or the sum of radii for non-bonded particles. The damping strength Γ is set to $50\sqrt{mu}/a$ which keeps the system athermal and is representative of the overdamped limit. Over the range of strain rates simulated, the kinetic energy is quickly dissipated such that inertia is unable to sustain crack propagation or granular rearrangement if mechanical loading were to stop. All other quantities in this article are dimensionless, scaled by the appropriate combination of a, m, and u.

Systems undergo pure shear where one box dimension contracts at a true strain rate labeled $\dot{\epsilon}$ while the other expands to preserve area. To reach large strains, simulations are fully-periodic and use Kraynik-Reinelt boundaries [68]. Simulations were run in LAMMPS [69, 70] which includes a recently added bonded particle model package.

During loading, the stress rises linearly with strain ϵ before cracks nucleate and grow at $\epsilon \approx 2\%$ causing the stress to drop as seen in Fig. 6. The resulting system, fractured and broken into pieces, then fluctuates around a smaller stress as granular fragments flow in shear. This average stress gradually decays on longer timescales as fragments continue to break into smaller pieces, as indicated by a decay in the number of bonds. Notably, this

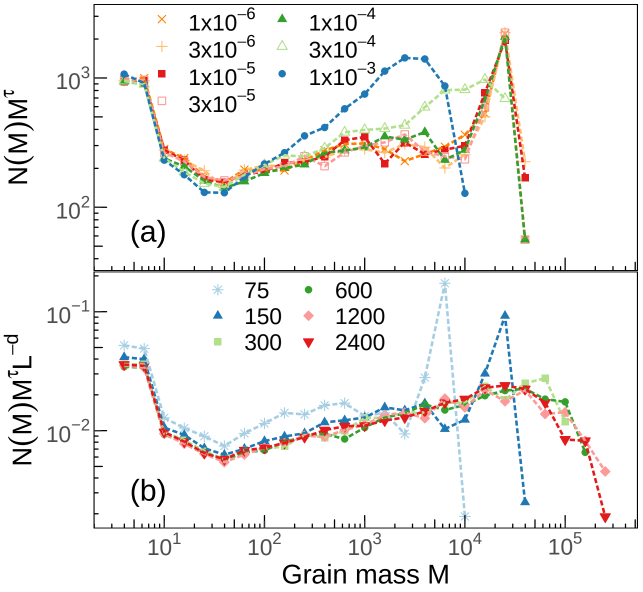

FIG. 7. (a) Scaled distributions $N(M)$ for a system of size $L = 150$ sheared at the indicated strain rates $\dot{\epsilon}$ to a strain $\epsilon = 100\%$. (b) Similar distributions with the dependence on L^d with $d = 2$ also removed for systems of the indicated sizes at $\dot{\epsilon} = 10^{-4}$ and $\epsilon = 100\%$.

decay is punctuated by bursts of rapid bond breakage as seen in the inset of Fig. 6. These events resemble crackling noise produced by intermittent avalanches in the yielding transition [44, 64, 71, 72]. This is not unexpected as avalanche-like bursts have been found in the propagation of cracks in heterogeneous materials [73, 74]. However, a different deformation protocol is required to accurately separate individual events and calculate a distribution of magnitudes [35, 36].

Appendix B: Additional finite-size effects and scaling

In this appendix, we both demonstrate how distributions transition between the QS and FR limits and how they can be roughly collapsed using scaling theories proposed in the main text. As previously mentioned, the shape of $N(M)$ changes with decreasing rate up until it reaches a limiting QS form at a value of $\dot{\epsilon}$ that decreases with increasing system size L. This is seen when comparing distributions at different $\dot{\epsilon}$ for $L = 150$ in Fig. 7(a) to previous data at $L = 2400$ in Fig. 3(b). In contrast to $L = 2400$ where $N(M)$ evolves with decreasing rate down to $\dot{\epsilon} = 3 \times 10^{-6}$, at $L = 150$ $N(M)$ converges by $\dot{\epsilon} = 10^{-4}$. This behavior is also seen in Fig. 7(b) where $N(M)$ at $\dot{\epsilon} = 10^{-4}$ has a nontrivial dependence on L for $L < 300$ but simply scales as L^2 for $L \geq 300$ where the number of grains grows linearly with the area of the system. As in Fig. 4, we see a spike emerge in the number of grains near M_{cut} in small systems as they enter the QS limit. The reduction in the steepness of $N(M)$ at large $\dot{\epsilon}$ is also preserved at small L when entering the QS limit, although this is clouded by the changing shape of $N(M)$ near M_{cut} and is quite subtle in Fig. 4. Similar behavior is seen when comparing distributions at other cross sections of rate or system size.

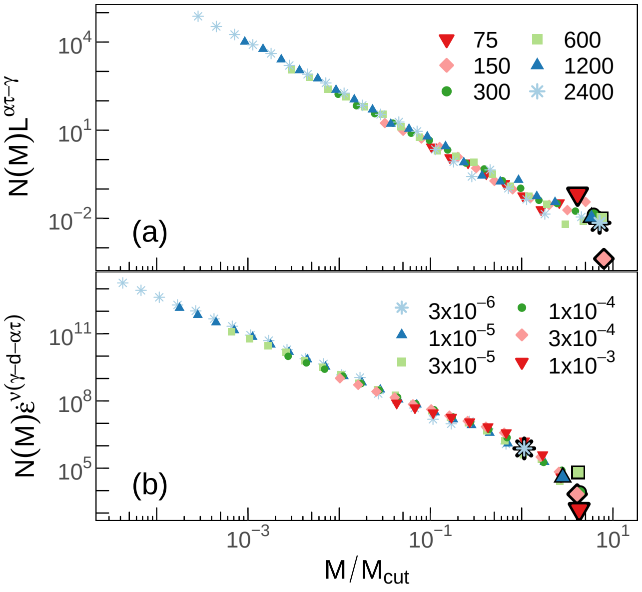

FIG. 8. (a) Collapsed QS distributions from Fig. 4 for $M > M_{\mathrm{min}}$ using the procedure in Eq. (1) using a value of $M_{\mathrm{cut}} = L^{\alpha}$. (b) Similarly collapsed FR distributions from Fig. 3(b) using Eq. (2) and $M_{\mathrm{cut}} = \dot{\epsilon}^{-\nu\alpha}$. Exponents are taken from Table I. The largest mass of each dataset is enlarged for visibility.

As alluded to in the main text, the scaling theories in Eqs. (1) and (2) can be used to collapse distributions however deviations at small L and large $\dot{\epsilon}$ as well as limited statistics near M_{cut} make it difficult to assess the quality of the collapses and bound exponents. Nevertheless, QS distributions from Fig. 4 for different L are reasonably collapsed in Fig. 8(a) using exponents in Table I and the protocol in Eq. (1). Importantly, distributions are consistently cut off around a constant value of M/L^{α} for all L. As noted before, the spike in $N(M)$ near M_{cut} for L less than ~ 300 implies these systems are too small to satisfy the assumptions of Eq. (1).

Similarly, distributions in the FR limit for $L = 2400$ for different $\dot{\epsilon}$ from Fig. 3(b) are roughly collapsed in Fig. 8(b) using the procedure in Eq. (2). The evolution in the steepness of the distribution, which breaks assumptions used to derive Eq. (2) but becomes less prominent at smaller $\dot{\epsilon}$, obscures the collapse. Notably, however, distributions again go to zero near an equivalent value of $M\dot{\epsilon}^{\nu\alpha}$ for all $\dot{\epsilon} < 3 \times 10^{-6}$ where data at $\dot{\epsilon} = 3 \times 10^{-6}$ should not collapse as it is already transitioning to QS behavior (Fig. 5). Despite these complications, this process is still a useful test of exponents in Table I and is consistent with the predicted scaling of M_{cut} and $N(M)$.

---

[1] C. Marone and C. H. Scholz, J. Struct. Geol. **11**, 799 (1989).

[2] H. Kanamori and E. E. Brodsky, Reports Prog. Phys. **67**, 1429 (2004).

[3] D. P. O'Brien and R. Greenberg, Icarus **164**, 334 (2003).

[4] A. C. Palmer and T. J. O. Sanderson, Proc. R. Soc. A **433**, 469 (2006).

[5] M. Gherardi and M. C. Lagomarsino, Sci. Rep. **5**, 1 (2015).

[6] W. W. Chen, A. M. Rajendran, B. Song, and X. Nie, J. Am. Ceram. Soc. **90**, 1005 (2007).

[7] J. D. Hogan, L. Farbaniec, D. Mallick, V. Domnich, K. Kuwelkar, T. Sano, J. W. McCauley, and K. T. Ramesh, Int. J. Impact Eng. **102**, 47 (2017).

[8] K. T. Ramesh, L. Graham-Brady, W. A. Goddard, R. C. Hurley, M. Robbins, A. L. Tonge, A. Bhattacharjee, J. T. Clemmer, Q. Zeng, W. Li, Y. Shen, Q. An, and N. Mitra, J. Am. Ceram. Soc. **105**, 3043 (2022).

[9] A. Bhattacharjee, R. C. Hurley, and L. Graham-Brady, J. Am. Ceram. Soc. **105**, 3062 (2022).

[10] V. M. Kenkre, M. R. Endicott, S. J. Glass, and A. J. Hurd, J. Am. Ceram. Soc. **79**, 3045 (1996).

[11] R. C. Hurley, J. Lind, D. C. Pagan, M. C. Akin, and E. B. Herbold, J. Mech. Phys. Solids **112**, 273 (2018).

[12] X. Sun, A. Chauhan, D. D. Mallick, A. L. Tonge, J. W. McCauley, K. J. Hemker, J. C. LaSalvia, and K. Ramesh, J. Mech. Phys. Solids **143**, 104031 (2020).

[13] I. Einav, Proc. R. Soc. A **463**, 3021 (2007).

[14] M. B. Cil, R. C. Hurley, and L. Graham-Brady, J. Am. Ceram. Soc. **102**, 5524 (2019).

[15] M. B. Cil, Q. Zeng, R. C. Hurley, and L. Graham-Brady, J. Dyn. Behav. Mater. **6**, 472 (2020).

[16] A. Bhattacharjee, A. Bhaduri, R. Hurley, and L. Graham-Brady, Journal of Applied Mechanics **88**, 1 (2021).

[17] D. Grady and M. Kipp, Mech. Mater. **4**, 311 (1985).

[18] Z. Cheng and S. Redner, J. Phys. A **23**, 1233 (1990).

[19] C. K. C. Lieou, A. E. Elbanna, and J. M. Carlson, Phys. Rev. E **89**, 022203 (2014).

[20] J. Andrejevic, L. M. Lee, S. M. Rubinstein, and C. H. Rycroft, Nat. Commun. **12**, 1470 (2021).

[21] D. L. Turcotte, J. Geophys. Res. **91**, 1921 (1986).

[22] L. Oddershede, P. Dimon, and J. Bohr, Phys. Rev. Lett. **71**, 3107 (1993).

[23] H. A. Carmona, F. K. Wittel, F. Kun, and H. J. Herrmann, Phys. Rev. E **77**, 051302 (2008).

[24] F. K. Wittel, H. A. Carmona, F. Kun, and H. J. Herrmann, Int. J. Fract. **154**, 105 (2008).

[25] G. Timár, J. Blömer, F. Kun, and H. J. Herrmann, Phys. Rev. Lett. **104**, 095502 (2010).

[26] G. R. McDowell, Soils Found. **42**, 139 (2002).

[27] F. Altuhafi and M. Coop, Géotechnique **61**, 459 (2011).

[28] Y. Xiao, H. Liu, Q. Chen, L. Long, and J. Xiang, Granul. Matter **19** (2017).

[29] P. S. Iliev, F. K. Wittel, and H. J. Herrmann, Phys. Rev. E **99**, 012904 (2019).

[30] M. R. Coop, K. K. Sorensen, T. B. Freitas, and G. Georgoutsos, Géotechnique **54**, 157 (2004).

[31] J. A. Åström and H. J. Herrmann, Eur. Phys. J. B **5**, 551 (1998).

[32] P. Bak, C. Tang, and K. Wiesenfeld, Phys. Rev. A **38**, 364 (1988).

[33] B. A. Sun, H. B. Yu, W. Jiao, H. Y. Bai, D. Q. Zhao, and W. H. Wang, Phys. Rev. Lett. **105**, 035501 (2010).

[34] N. W. Hayman, L. Ducloué, K. L. Foco, and K. E. Daniels, Pure Appl. Geophys. **168**, 2239 (2011).

[35] K. M. Salerno, C. E. Maloney, and M. O. Robbins, Phys. Rev. Lett. **109**, 105703 (2012).

[36] K. M. Salerno and M. O. Robbins, Phys. Rev. E **88**, 062206 (2013).

[37] J. Barés, D. Wang, D. Wang, T. Bertrand, C. S. O'Hern, and R. P. Behringer, Phys. Rev. E **96**, 052902 (2017).

[38] P. J. Cote and L. V. Meisel, Phys. Rev. Lett. **67**, 1334 (1991).

[39] H. Ji and M. O. Robbins, Phys. Rev. B **46**, 14519 (1992).

[40] O. Perković, K. A. Dahmen, and J. P. Sethna, Phys. Rev. B **59**, 6106 (1999).

[41] M. Moura, K. J. Måløy, and R. Toussaint, EPL **118** (2017).

[42] J. T. Clemmer and M. O. Robbins, Phys. Rev. E **100**, 042121 (2019).

[43] D. S. Fisher, Phys. Rep. **301**, 113 (1998).

[44] J. P. Sethna, K. A. Dahmen, and C. R. Myers, Nature **410**, 242 (2001).

[45] J. Lin, E. Lerner, A. Rosso, and M. Wyart, Proc. Natl. Acad. Sci. U.S.A **111**, 14382 (2014).

[46] C. J. Allègre, J. L. Le Mouel, and A. Provost, Nature **297**, 47 (1982).

[47] E. Perfect, Eng. Geol. **48**, 185 (2002).

[48] O. Tsoungui, D. Vallet, and J. C. Charmet, Powder Technol. **105**, 190 (1999).

[49] O. Ben-Nun and I. Einav, Philos. Trans. R. Soc. A **368**, 231 (2010).

[50] A. Lisjak and G. Grasselli, J. Rock Mech. Geotech. Eng. **6**, 301 (2014).

[51] C. E. Maloney and M. O. Robbins, Chaos **17**, 041105 (2007).

[52] R. C. Hurley and D. C. Pagan, International Journal of Solids and Structures **168**, 26 (2019).

[53] See Supplemental Material for a brief description of results from three-dimensional simulations run using generalized Kraynik-Reinelt boundary conditions [54].

[54] T. A. Hunt, Mol. Simul. **42**, 347 (2016).

[55] D. Cereceda, L. Graham-Brady, and N. Daphalapurkar, Int. J. Impact Eng. **99**, 85 (2017).

[56] J. Lankford, J. Mater. Sci. Lett. **15**, 745 (1996).

[57] J. A. Åström, B. L. Holian, and J. Timonen, Phys. Rev. Lett. **84**, 3061 (2000).

[58] S. Levy and J. F. Molinari, J. Mech. Phys. Solids **58**, 12 (2010).

[59] A. Clauset, C. R. Shalizi, and M. E. J. Newman, SIAM Rev. **51**, 661 (2009).

[60] O. Narayan and D. S. Fisher, Phys. Rev. B **48** (1993).

[61] P. Chauve, P. Le Doussal, and K. J. Wiese, Phys. Rev. Lett. **86**, 1785 (2001).

[62] R. A. White and K. A. Dahmen, Phys. Rev. Lett. **91**, 085702 (2003).

[63] J. T. Clemmer, K. M. Salerno, and M. O. Robbins, Phys. Rev. E **103**, 042605 (2021).

[64] J. T. Clemmer, K. M. Salerno, and M. O. Robbins, Phys. Rev. E **103**, 042606 (2021).

[65] C. E. Maloney and M. O. Robbins, J. Phys. Condens.

Matter **20**, 244128 (2008).

[66] F. Wittel, F. Kun, H. Herrmann, and B. Kröplin, Phys. Rev. Lett. **93**, 035504 (2004).

[67] R. D. Groot and P. B. Warren, J. Chem. Phys. **107**, 4423 (1997).

[68] A. Kraynik and D. Reinelt, Int. J. Multiph. Flow **18**, 1045 (1992).

[69] S. Plimpton, J. Comput. Phys. **117**, 1 (1995).

[70] A. P. Thompson, H. M. Aktulga, R. Berger, D. S. Bolintineanu, W. Michael Brown, P. S. Crozier, P. J. in 't Veld, A. Kohlmeyer, S. G. Moore, T. D. Nguyen, R. Shan, M. Stevens, J. Tranchida, C. Trott, and S. J. Plimpton, Comput. Phys. Commun. , 108171 (2021).

[71] M. C. Kuntz and J. P. Sethna, Phys. Rev. B **62**, 11699 (2000).

[72] E. K. Salje and K. A. Dahmen, Annu. Rev. Condens. Matter Phys. **5**, 233 (2014).

[73] G. Timár and F. Kun, Phys. Rev. E **83**, 046115 (2011).

[74] J. Barés, D. Bonamy, and A. Rosso, Phys. Rev. E **100**, 023001 (2019).